ALGINATE AND CHITOSAN COMPOSITE SCAFFOLD COATED WITH CURCUMIN NANOPARTICLES FOR DIABETIC WOUND HEALING

MUSA AYRAN[1,2], ZEKIYE AKDAG[1,2], SONGUL ULAG[1,3]*, OGUZHAN GUNDUZ[1,3]
[1]*Center for Nanotechnology & Biomaterials Application and Research (NBUAM), Marmara University, Turkey*
[2]*Department of Metallurgical and Materials Engineering, Institute of Pure and Applied Sciences, Marmara University, Turkey*
[3]*Metallurgical and Materials Engineering, Faculty of Technology, Marmara University, Turkey*

Diabetic wounds pose a significant challenge in clinical settings, primarily due to uncontrolled blood sugar levels and compromised immune systems observed in diabetes mellitus. Curcumin (CUR), a well-known anti-inflammatory and antioxidant agent, has shown potential for wound regeneration. However, its limited bioavailability and stability necessitate the development of a novel scaffold to overcome these limitations. In this study, we investigated the wound-healing properties of extracted CUR from Curcuma longa rhizomes and their combination with organic polymers by developing and evaluating a biomimetic composite 3D scaffold specifically designed for diabetic wounds. Incorporating CUR and Ethyl cellulose (EC) nanoparticles onto Alginate and Chitosan (SA/CS) scaffolds was achieved through the electrospraying method, resulting in an average particle size of 784±35.1 nm for CUR/EC nanoparticles. The interaction between different concentrations of CUR1 and CUR3 (1mg/1ml and 3mg/1ml) with EC on scaffolds was analyzed using FTIR spectroscopy, providing insights into the chemical composition of the scaffolds. The structural properties of the scaffolds and nanoparticles were examined to assess their morphological characteristics. Furthermore, the swelling and degradation behaviors of the scaffolds were investigated under in vitro conditions. The release profile of CUR was determined, and cytotoxicity testing was performed on the L929 cell line using an MTT assay to evaluate the biocompatibility of CUR/EC-coated scaffolds, as indicated by viable and proliferating cells in vitro study. In addition, the potential of CUR/EC-coated scaffolds to support tissue regeneration was evaluated using a DAPI staining assay and scanning electron microscopy (SEM).

Keywords: *Alginate; chitosan; curcumin; electrospraying; wound healing; 3D printing.*

1. Introduction

Chronic wounds, which represent a prevalent complication of diabetic wound healing, have become a significant public health concern of substantial magnitude [1]. Emerging evidence suggests that the impaired healing of chronic diabetic wounds is primarily attributed to heightened inflammatory responses, oxidative stress, and persistent infections [2]. In order to confront these challenges, there has been a growing research focus on tissue engineering materials, which have garnered widespread application as potential interventions. Diabetic wounds often become trapped in a persistent inflammatory phase characterized by an ongoing influx of neutrophils. These neutrophils release cytotoxic enzymes, free radicals, and inflammatory mediators, leading to significant collateral damage to the surrounding tissue [3]. The healing process of diabetic wounds poses a formidable challenge, necessitating a comprehensive and intricate treatment approach to attain full recovery. Amidst many surgical and non-surgical modalities available for managing chronic wounds, wound dressings emerge as one of the prevailing methodologies[4].

The scaffolds serve as a supportive framework within the diabetic wound microenvironment, exerting regulatory influence over cellular behaviors such as proliferation, migration, and differentiation. By providing instructive cues, these scaffolds play a vital role in facilitating efficient wound closure and optimizing the healing process [5]. Scaffolds and nanoparticle-loaded scaffolds have gained considerable popularity in the field of tissue engineering, particularly in the context of diabetic wound healing, due to their ease of manufacturing and vast potential for applications. The scaffolds also feature porous microstructures endowed with cell-binding sites, facilitating cellular infiltration and adhesion. Furthermore, they facilitate the diffusion of essential nutrients and metabolites, possess adjustable degradation mechanisms, and function as reservoirs capable of retaining bioactive agents. These bioactive agents, in turn, play a crucial role in triggering the activation of innate tissue repair mechanisms [6]. Alginate and chitosan were chosen as biomaterials for 3D-printed scaffolds due to their exceptional biocompatibility and desirable mechanical properties [7]. Researchers Baruch and Machluf [8] elucidated that the alginate-chitosan system exhibited favorable mechanical characteristics and demonstrated prolonged viability for cell encapsulation.

Curcumin(CUR), a natural polyphenol derived from the rhizome of *Curcuma longa*, has garnered significant research interest due to its established neuroprotective effects and potent antioxidant properties [9]. Moreover, its traditional usage as a medicinal remedy for inflammation and wound healing has been well-documented over time [10].

*Autor corespondent/*Corresponding author*,
E-mail: songul.ulag@marmara.edu.tr

The topical administration of CUR has been reported to play a significant role in wound healing mechanisms. In the realm of diabetes research, CUR, the most active constituent of turmeric, has attracted scientific attention as a promising therapeutic agent for experimental diabetes and managing diabetes-related complications in patients [11]. The molecular structure of CUR manifests a multifaceted capacity to target diverse pathological conditions, thereby rendering it a potential candidate for translation into therapeutic or nutraceutical applications. CUR possesses the capability to modulate oxidative and inflammatory imbalances, address metabolic syndrome, ameliorate arthritis, alleviate anxiety, and manage hyperlipidemia [12].

Ethyl cellulose(EC), an ether cellulose polymer characterized by its water-insolubility, non-biodegradability, and ability to form robust, resilient films with favorable adhesion properties even at low concentrations, is a widely employed material for the production of polymeric nanoparticles. [13]. EC nanoparticles have been a notable surge in interest regarding the utilization of EC nanoparticles as stabilizers [14]. Specifically, EC nanoparticles have been extensively studied for their application in pharmaceutical encapsulation [15], [16] owing to their low toxicity, environmentally responsible nature [17], and notable capability to stabilize foams [18]. This has contributed to the growing interest in exploring the potential of EC nanoparticles as a versatile and promising stabilizing agent.

Biopolymeric particles offer significant potential for enhancing the stability of bioactive molecules, protecting them from degradation, improving their absorption, and facilitating targeted delivery [19]. Moreover, these particles can serve as efficient carriers for controlled release, enabling sustained and controlled release of their encapsulated ingredients [20]. Furthermore, the classification of biopolymeric particles is typically based on their preparation methods, such as inclusion complex formation, as well as their nano-dimensions, which encompass various forms such as nanofibers, nanospheres, and others [21]. These versatile particles provide a promising platform for advanced drug delivery systems and have gained considerable attention in the field of biomedical research. Due to these inherent properties, incorporating nanoparticles onto the scaffold emerges as a notably superior and distinct approach compared to simply mixing nanoparticles within the scaffold matrix. Through the exploration of this approach, we anticipate that the subsequent release kinetics will demonstrate the rapid release. In our study, we utilized electrospraying to encapsulate CUR/EC nanoparticles onto 3D printed SA/CS scaffolds, aiming to evaluate their potential as therapeutic agents for diabetic wound healing. To assess the impact of CUR/EC-coated scaffolds on cellular responses, we conducted various analyses, including cytotoxicity assessment, fluorescence imaging, and SEM. These analyses allowed us to investigate the effects of encapsulated CUR/EC nanoparticles on cell viability, proliferation, and attachment within the scaffolds. Furthermore, we examined the release kinetics, swelling behavior, degradation rate, and mechanical properties of the CUR/EC-coated scaffolds. By investigating these characteristics, we gained insights into the scaffold's ability to deliver CUR/EC-coated and respond to the wound site. By employing these multidimensional analyses, we aimed to better understand the therapeutic potential of CUR/EC-coated scaffolds for diabetic wound healing. The findings from our study contribute to the advancement of wound healing strategies and may pave the way for the development of effective therapies for diabetic patients.

2. Materials and Methods

2.1. Materials

Sigma-Aldrich (Istanbul, Turkey) provided SA that had an average molecular weight of 216.121 g/mol, while Merck (Darmstadt, Germany) supplied calcium chloride dihydrate ($CaCl_2.2H_2O$), which was used as a crosslinker. EC used as a carrier (Ref. 433837-250G, viscosity of 46 cP, CAS 9004-57-3) was purchased from Sigma Aldrich Chemical (St. Louis, MO, USA). CS of molecular weight (Mw) 45 KDa was purchased from Sigma-Aldrich (448877–250G). Ethanol (%99.9 purity, v/v) was purchased from Sigma-Aldrich (UK). Dulbecco's modified eagle medium and Ham's F-12 medium (DMEM/F-12), fetal bovine serum (FBS), penicillin/streptomycin solution, and Trypsin-EDTA (0.25%) were purchased from Gibco. Phosphate-buffered saline (PBS), dimethyl sulfoxide (DMSO), 4',6-diamidino-2-phenylindole (DAPI), phenazine methosulfate (PMS), and 10% formalin were obtained from Sigma-Aldrich. 2,3-bis(2-methoxy-4-nitro-5-sulfophenyl)-2H-tetrazolium-5-carboxanilide (XTT) was purchased from Biomatik.

2.2.Preparation of CUR Extracts

Curcuma longa rhizomes were acquired from a supplier located in the Istanbul province of Turkey. To ensure the preservation of their bioactive constituents, the rhizome parts of C. longa were subjected to a controlled drying process using an oven set at 105 °C. Subsequently, the dried rhizomes were sieved to obtain a finely powdered extract, thereby promoting a more homogeneous composition. To maintain the integrity and potency of the plant material, the obtained powder was stored in a refrigerated environment, mitigating the potential degradation caused by moisture or other

detrimental factors. Subsequently, a soxhlet extraction method was employed to extract the desired constituents from the plant material. The powdered plant material was carefully packed into a thimble, which was then inserted into the soxhlet apparatus. For the extraction process, acetone was chosen as the solvent. The acetone solvent was gradually introduced into the Soxhlet apparatus, allowing for the extraction of bioactive compounds from the plant material over an extended period. This extraction process was conducted for 8 hours, maintaining a constant temperature of 60 °C to optimize the extraction efficiency. Following the conclusion of the extraction process, the resulting extract underwent a concentration step employing a vacuum-assisted rotary evaporator. This sophisticated methodology enabled the careful elimination of the acetone solvent under precisely controlled conditions, specifically at a temperature of 35 °C [22].

2.3.Preparation of solutions

Two separate solutions were prepared: one for the synthesis of nanoparticles through electrospraying and another for the fabrication of 3D-printed scaffolds.

For the synthesis of nanoparticles, precise proportions of CUR were meticulously incorporated into an ethanol/water (80:20) solution containing 5% (w/v) EC. Different concentrations of CUR were used 1mg/1ml (CUR1/EC) and 3mg/1ml (CUR3/EC). The optimization of EC concentration in this study was conducted based on previous research findings [14]. The CUR was methodically dispersed within the solution using gentle stirring, ensuring the achievement of a homogeneous mixture at room temperature.

Regarding the SA/CS included solution was meticulously formulated for the purpose of 3D printing scaffolds. The scaffold formulation was prepared with the precise incorporation of 8% (w/v) SA and 0.5% (w/v) CS in 10ml acetic acid at room temperature with a magnetic stirrer. The acetic acid solution served as a suitable solvent for the polymer blend, ensuring proper dissolution and homogenization of the SA and CS [23]. Calcium chloride was used as a crosslinking agent for a 3D printed SA/CS scaffold.

2.4. Electrospraying of Nanoparticles for Integration with 3D Printed Scaffold

The scaffolds were designed using computer-aided design (CAD) software, specifically SolidWorks®, with dimensions of 20 × 20 × 1 mm^3 and an average porosity of approximately 75%. A preliminary scaffold structure was created in the software and then converted into an STL (stereolithography) file, which is the required format for 3D printing. The designed scaffold in STL format was imported into the RepetierHost program, which facilitated the printing process using a 3D printer (AXO-A3, Axolotl Biosystems). During scaffold production, the fill density was set at 70%, ensuring a balance between structural integrity and porosity. A nozzle with a diameter of 0.35 mm was employed, and the printing speed was set to 240 mm/min for the control SA scaffolds. The scaffolds were printed in 8 layers, maintaining consistent layer thickness throughout. For the internal structure of the scaffolds, a rectilinear infill pattern with a 90-degree fill angle was chosen. This pattern and square pore morphology were selected based on previous studies [24], [25], which demonstrated that square pores offer superior compressive strength and modulus compared to other pore morphologies. The mentioned parameters, such as infill pattern and pore morphology, were determined through optimization studies, ensuring the scaffolds' mechanical properties met the desired specifications. The consolidation and removal of the printed scaffold were facilitated by utilizing a $CaCl_2$ crosslinker solution. The scaffolds were immersed in the $CaCl_2$ solution for a duration of 15 minutes to allow for effective consolidation. Following the immersion, the scaffolds were carefully dried until complete. This process allowed for the safe and intact transfer of the scaffolds for subsequent spraying procedures.

The CUR and 5% (w/v) EC solution is loaded into a syringe or a reservoir attached to a syringe pump. The solution is then connected to a conductive needle or nozzle. A high voltage is applied between the needle/nozzle and a grounded collector or target substrate through an electrospinning device (NS24, InovensoCo, Turkey). This creates an electric field at the needle/nozzle tip. The voltage was set at 18 kV, and the collector was covered with aluminum foil to collect the electrosprayed droplets, maintaining a distance of 12 cm between them. The syringe pump (NE-300, USA) was set to a flow rate of 0.5 mL/h, and the electrospraying process was initiated. The applied electric field caused the formation of charged droplets containing the CUR1/EC and CUR3/EC nanoparticles. The propelled droplets were directed toward the SA/CS scaffolds situated on the glass slide, which was positioned on the aluminum foil. Simultaneously, the solvent underwent evaporation during the flight of the droplets, ensuring the deposition of the desired material onto the scaffold surfaces. The experimental design and methods utilized in this study are visually depicted in Figure 1.

2.5.Characterizations

2.5.1.Morphological Characterizations of the Scaffolds

To gain insight into the surface morphology of the scaffolds and nanoparticles, we employed SEM using an EVA MA 10 ZEISS instrument (Jena, Germany).

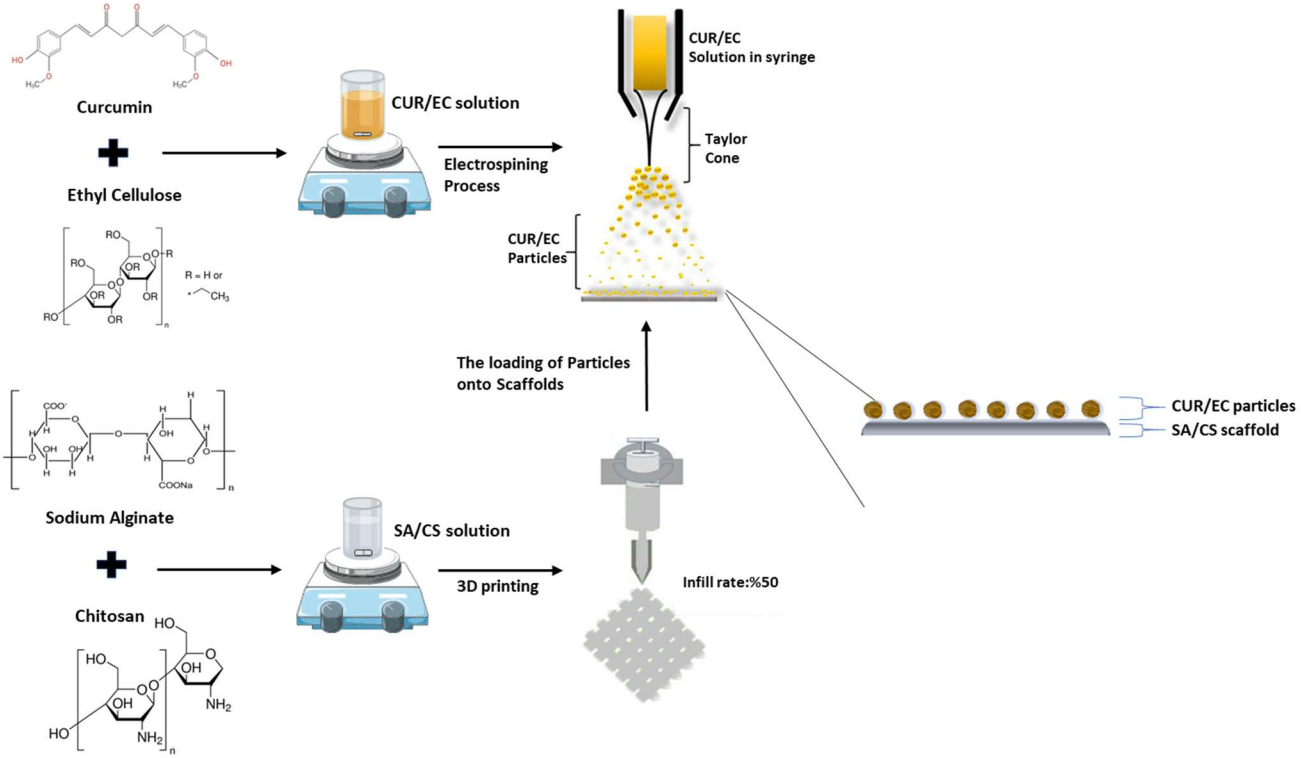


Fig. 1 - Graphical representation of the experimental design and methods employed in this study.

Prior to imaging, the scaffolds and nanoparticles underwent gold (Au) and palladium (Pd) coating in a sputter coating machine (Quorum SC7620, Quorum Technologies Ltd., East Sussex, UK) for 120 seconds, ensuring conductivity and high-resolution image quality. The resulting micrographs were then analysed using Analysis5 software from Olympus (Münster, Germany) to determine the average pore size of each scaffold and the size of nanoparticles.

2.5.2.Chemical Characterizations of the Scaffolds

The scaffolds were analysed for molecular and chemical interactions through the use of fourier transform infrared spectroscopy (FTIR) using a Jasco FT/IR 4700 instrument (Tokyo, Japan). The spectra were captured at a resolution of 4 cm^{-1} over a range of wavelengths from 450 to 4000 cm^{-1}.

2.5.3. Thermal Characterizations of the Scaffolds

The thermal behavior of the scaffolds was analyzed using differential scanning calorimetry (DSC) (Shimadzu, Japan). Each scaffold was placed in an aluminum pan and subjected to a temperature range of 25°C to 400°C, allowing for the measurement of thermal properties such as glass transition temperature (T_g) and melting temperature (T_m). The analysis was performed at a scanning rate of 10°C/min by monitoring the heat flow required to maintain a constant temperature.

2.5.4. Mechanical Properties of the Scaffolds

The tensile strength and elongation at the break of the scaffolds were measured using a Shimadzu (EZ-LX, Beijing, China) tensile testing machine. All scaffolds were measured and placed uniaxially between the upper and lower sections of the device for testing. Mean tensile strength and strain values were calculated by conducting triplicate measures of each scaffold to ensure the precision and reliability of data.

2.5.5.In vitro release of CUR

For the *in vitro* drug release analysis, the CUR solution was prepared in PBS at six different concentrations (0.2, 0.4, 0.6, 0.8, and 1 mg/ml) at a wavelength range of 300-460 nm. This allowed us to accurately determine the concentrations of the CUR nanoparticles on scaffolds, a standard calibration curve was prepared prior to the release test. CUR/EC-coated scaffolds were first cut into 5-mg pieces and placed into eppendorf tubes. Then, 3 mL of PBS solution at pH 7.4 and 37 °C was added to the tubes, and they were placed in a shaking incubator operating at 37 °C and 200 rpm for the test duration. At predetermined intervals, 3 ml of the PBS solution was withdrawn from the tubes and measured using a UV-vis spectrophotometer at 248 nm. After each measurement, 3 mL of fresh PBS was added to the tubes to maintain the release. The drug release test was conducted for 600 min to obtain a comprehensive understanding of the drug release behavior of the scaffolds. The Shimadzu UV-3600 spectrophotometer (Japan), which has high

accuracy and sensitivity, was utilized to ensure precise measurements and reliable results.

2.5.6. CUR release kinetics

Various mathematical models, namely the zero-order, first-order, Higuchi, and Hixson-Crowell models, were employed to analyze the drug release kinetics from scaffolds [26]. The fractional amount of drug release at a specific time is represented by Q in equations (1) through (4). Each equation uses a different set of kinetic constants, namely K_o, K_1, K_{HC} and K_H for the zero-order, first-order, Hixson-Crowell, and Higuchi, respectively.

$$Q = K_o t \quad (1)$$

$$\mathrm{In}\,(1-Q) = -K_1 t \quad (2)$$

$$Q_{1/3} = K_{HC} t \quad (3)$$

$$Q = K_H t^{0.5} \quad (4)$$

2.5.7. Swelling and Degradation Behaviors of Scaffolds

The swelling and degradation properties of scaffolds were assessed through a series of tests. To determine the swelling properties, scaffolds were immersed in PBS solution with a pH of 7.4 and placed in a thermal shaker (BIOSAN TS-100) at 37°C. The initial weights of the scaffolds were recorded, and the wet weights were measured daily. This allowed for the calculation of the swelling ratio, which was used to evaluate the capacity of the scaffolds to absorb fluids. The swelling value, denoted as S, was determined through the utilization of equation (5)[27]:

$$S = \frac{W_w - W_o}{W_o} \times 100 \quad (5)$$

The variable W_w represents the weight of the samples after swelling, while W_o denotes the weight of the samples before the swelling process.

The degradation properties of the scaffolds were determined by monitoring changes in their morphology and mass over time. The degradation test was performed in PBS solution (pH 7.4) at 37°C. At specific time intervals, the dried weights of the scaffolds were measured to evaluate their degradation behavior. The degradation value (D) was determined using equation (6):

$$D = \frac{W_1 - W_2}{W_1} \times 100 \quad (6)$$

This equation involves the weights of the scaffolds before and after degradation, represented by W_1 and W_2, respectively.

2.5.8. Cell culture and imaging

L929 mouse fibroblast cells (ATCC; CCL-1™) were cultured in DMEM/F-12 supplemented with 10% FBS and 1% penicillin/streptomycin under standard conditions: 37°C temperature and a 5% CO_2 incubator. The culture medium was refreshed every 2-3 days, and cell growth and adhesion were monitored using an inverse-phase contrast microscope (BEL, INV100). Once the cells reached a 70-80% confluent monolayer, they were detached from the culture flask using a trypsin/EDTA solution. The cell suspension was then centrifuged at 1000 rpm for 5 minutes, and the cells were resuspended in the culture medium. Subsequently, the cells were seeded into 96-well plates at a density of 1×10^4 cells/well and maintained in a humidified incubator at 37°C with 5% CO_2 for 24 hours. For the indirect cell viability assay, the scaffolds were first sterilized using overnight UV light exposure. After sterilization, the scaffolds were placed in a growth medium containing DMEM/F12 with 10% FBS and 1% penicillin/streptomycin. The scaffolds were then incubated with the medium for 1, 3, and 7 days in a 37°C, 5% CO_2 incubator. Following incubation, the scaffold medium was collected and cultured with L929 mouse fibroblast cells at 37℃, 5% CO_2, for 24 hours according to ISO Standard 10993-5[28]. Cells were incubated with an XTT solution containing DMEM/F12 and PMS for 4 hours in a dark environment, and the absorbance values were measured at 450 nm wavelength using an ELISA microplate reader (Lab-Line Instr., Inc.). The percentage of cell viability was calculated using the following equation (7):

$$\text{Cell viability}\ (\%) = \frac{\text{Mean optical density of samples}}{\text{Mean optical density of control}} \times 100 \quad (7)$$

DAPI staining was utilized to assess the adherence of L929 fibroblast cells on scaffolds. L929 fibroblast cells were seeded onto scaffolds at a density of 1×10^4 cells/well and incubated with the scaffolds for 1, 3, and 7 days. Following the incubation period, the cell growth medium was removed. The scaffolds were then fixed with a 10% formalin solution at room temperature for 30 minutes and subsequently rinsed with PBS. Following fixation, each sample was stained with DAPI solution for 30 minutes at 37℃ 5% CO_2 incubator and examined under an inverted fluorescent microscope (BEL, INV100-FL)[29].

2.5.9.Statistical Analysis

The experiment was conducted with three repetitions for each group, and the data were presented as the mean ± standard deviation (SD). A comparison between the means of the sample and control groups was performed using an unpaired Student's t-test. Statistical analysis was carried out using GraphPad software (GraphPad Inc., CA, USA). Differences were considered statistically significant if $p < 0.05$*, $p < 0.005$**, and $p < 0.001$*** compared to the control.

3.Results and Discussion

3.1. Morphological behaviors of scaffolds

Pores' dimensions and architectural configuration constitute critical parameters in the context of tissue scaffold utilization. 3D printed porous scaffold facilitates cell adhesion and

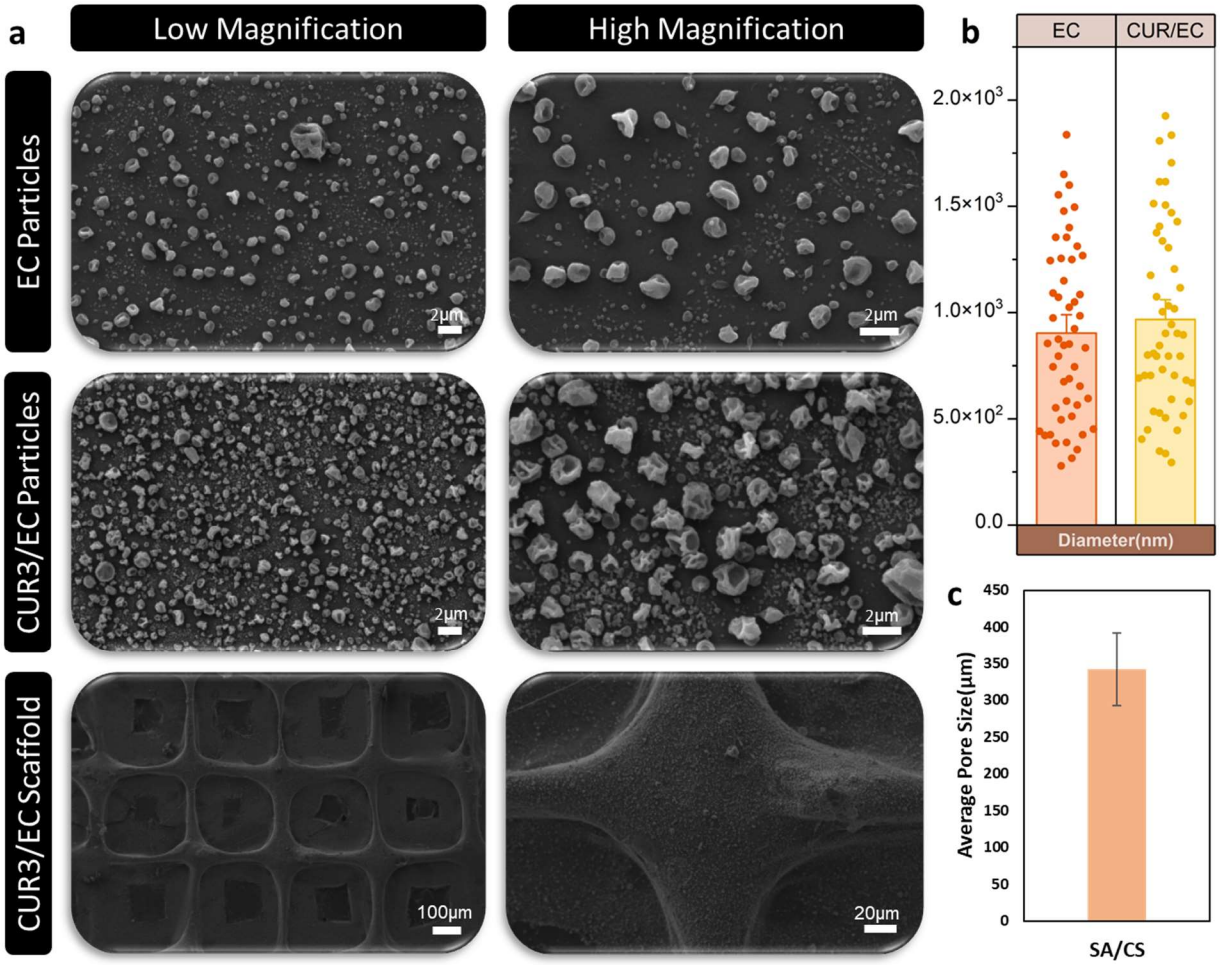


Fig. 2 - The figure showcases scanning electron microscopy (SEM) images capturing the morphology and structure of both nanoparticles and CUR/EC-coated scaffolds (a). A detailed analysis of the nanoparticles reveals their particle size distribution (b), while the pore size of the scaffolds is depicted (c), providing valuable insights into the overall architecture and porosity of the constructs.

proliferation while promoting cellular migration towards the regenerative sites during the wound-healing cascade. The presence of open and interconnected pores assumes paramount significance, as it ensures mechanical support, cellular nourishment, gas permeability, and the effective elimination of toxic by-products from the surrounding tissues [30]. Elevated porosity levels are conducive to enhanced nutrient transport within tissues yet concurrently lead to diminished structural density due to compromised mechanical stability. Selecting optimal pore size values for tissue scaffolds poses a formidable task owing to the inherent variability across diverse cell types and tissue compositions. Nevertheless, certain ranges of pore sizes have been suggested as potential optima for specific cell and tissue categories [25]. The researchers observed that the scaffold section characterized by a certain pore size range of 186–200 μm exhibited superior fibroblast growth [31]. To facilitate effective cell seeding within the scaffold, employing a scaffold with suitable porosity that allows for sufficient space is advisable. This recommendation ensures optimal cell integration and proliferation within the scaffold, enhancing its applicability for biomedical applications [32].

Representative SEM images of CUR3/EC nanoparticles and CUR3/EC scaffold are depicted in Figure 2(a). Figure 2 (b, c) presents the particle sizes of the EC, CUR3/EC nanoparticles and the average pore size of CUR3/EC scaffold. The CUR3/EC nanoparticles are utilized in the SA/CS scaffold. The average particle size of EC, CUR3/EC nanoparticles, and the pore size of the scaffolds were assessed via SEM, yielding measurements of 697±20 nm, 784±35.1 nm, and 347±52 μm, respectively. In particular, the morphological characteristics of the drug at a high concentration were thoroughly examined to assess the irregularity of nanoparticle sizes resulting from agglomeration and variations in particle size upon the addition of CUR to EC particles. Including CUR led to noticeable changes in the average particle size, and identifying structural disparities provides insights into the encapsulation process. This investigation sheds light on the formation of encapsulated CUR within the nanoparticles. The analysis reveals the uniform and consistent distribution of CUR3/EC nanoparticles throughout the SA/CS scaffolds. This observation confirms the successful coating and

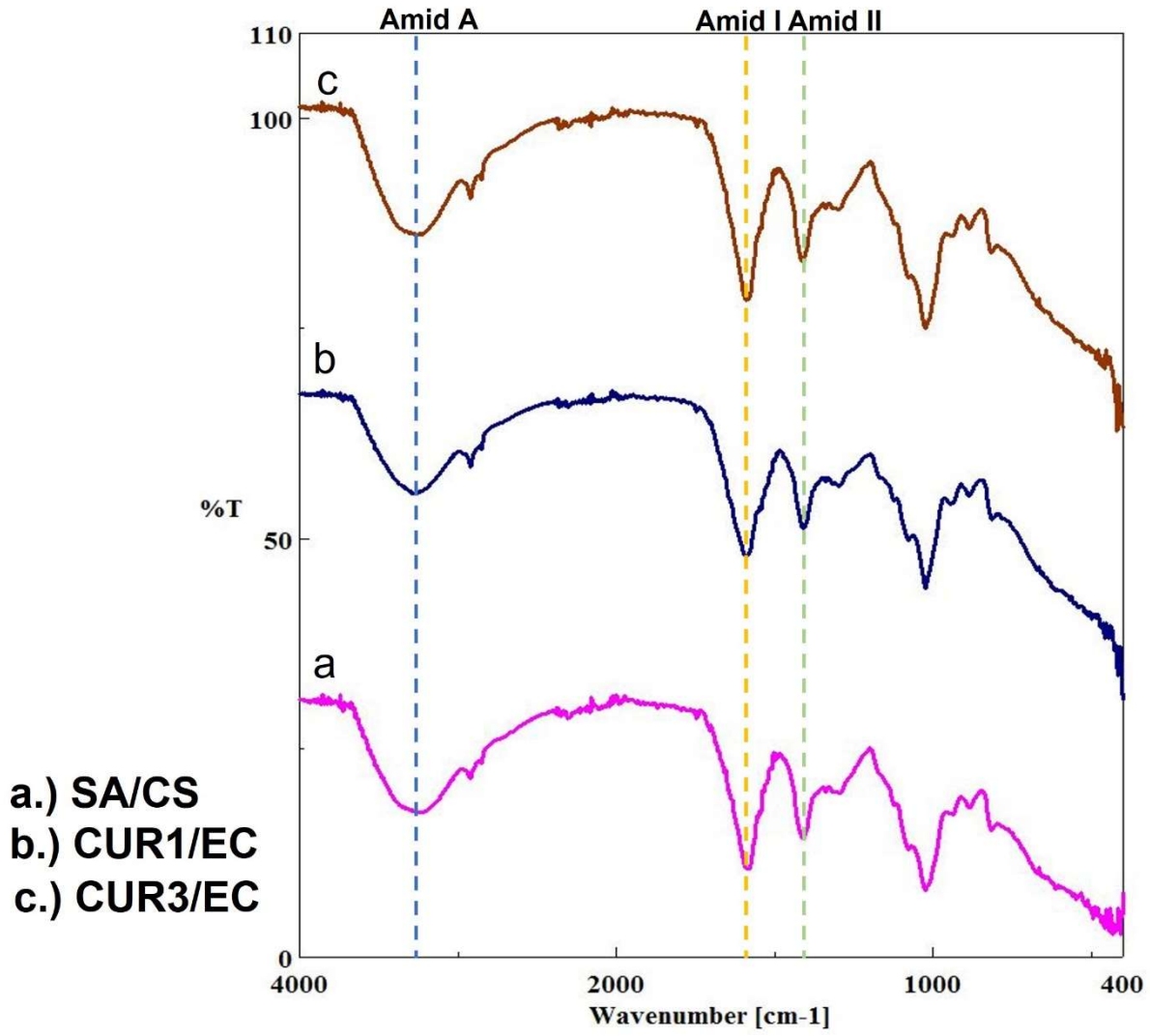


Fig. 3 - FTIR spectra comparison of SA/CS scaffold (a), CUR1/EC-coated and CUR3/EC-coated scaffolds (b, c), showing characteristic peaks for the functional groups present in each scaffold.

dispersion of CUR3/EC nanoparticles on the scaffold's surface.

3.2. FT-IR spectrophotometric analysis

FTIR analysis was conducted to explore the chemical and molecular structures of the CUR/EC-coated scaffolds, and the resulting spectrum is illustrated in Figure 3. This analysis revealed distinctive peaks in the infrared spectrum of scaffolds, demonstrating their molecular vibrational characteristics. In contrast to the morphological characteristics of the scaffolds, minimal disparity exists in their chemical compositions. The spectral patterns of CUR/EC-coated scaffolds in the analyzed regions are more similar to those SA/CS scaffolds. It is possible to observe the characteristic peaks of CUR/EC-coated and SA/CS scaffolds overlapped in certain regions of the spectrum. This overlapping phenomenon can be attributed to the similarities in the chemical functional groups present in CUR/EC and SA/CS, such as carbonyl, hydroxyl, and aromatic groups. Scaffolds exhibited a peak at 3350 cm^{-1}, corresponding to the O–H stretching vibration, and the spectrum is a common occurrence in polymeric systems due to the polymeric association of hydroxyl groups. Additionally, a peak at 1640 cm^{-1} was observed, indicating the stretching vibration of C=O (Amide I). Another peak at 1530 cm^{-1} was indicative of vibration N-H bending (Amide II). Furthermore, an aromatic (C=C) stretching vibration was identified at 1427 cm^{-1}, while a peak at 1262 cm^{-1} represented the bending vibrations of the C–O bond in the phenolic band of scaffolds. These findings provide valuable insights into scaffolds' molecular structure and functional groups. At 1033 cm^{-1}, a peak was observed, indicating the stretching vibration of the (C–O–C) bond, which aligns with the findings reported in the literature [33], [34].

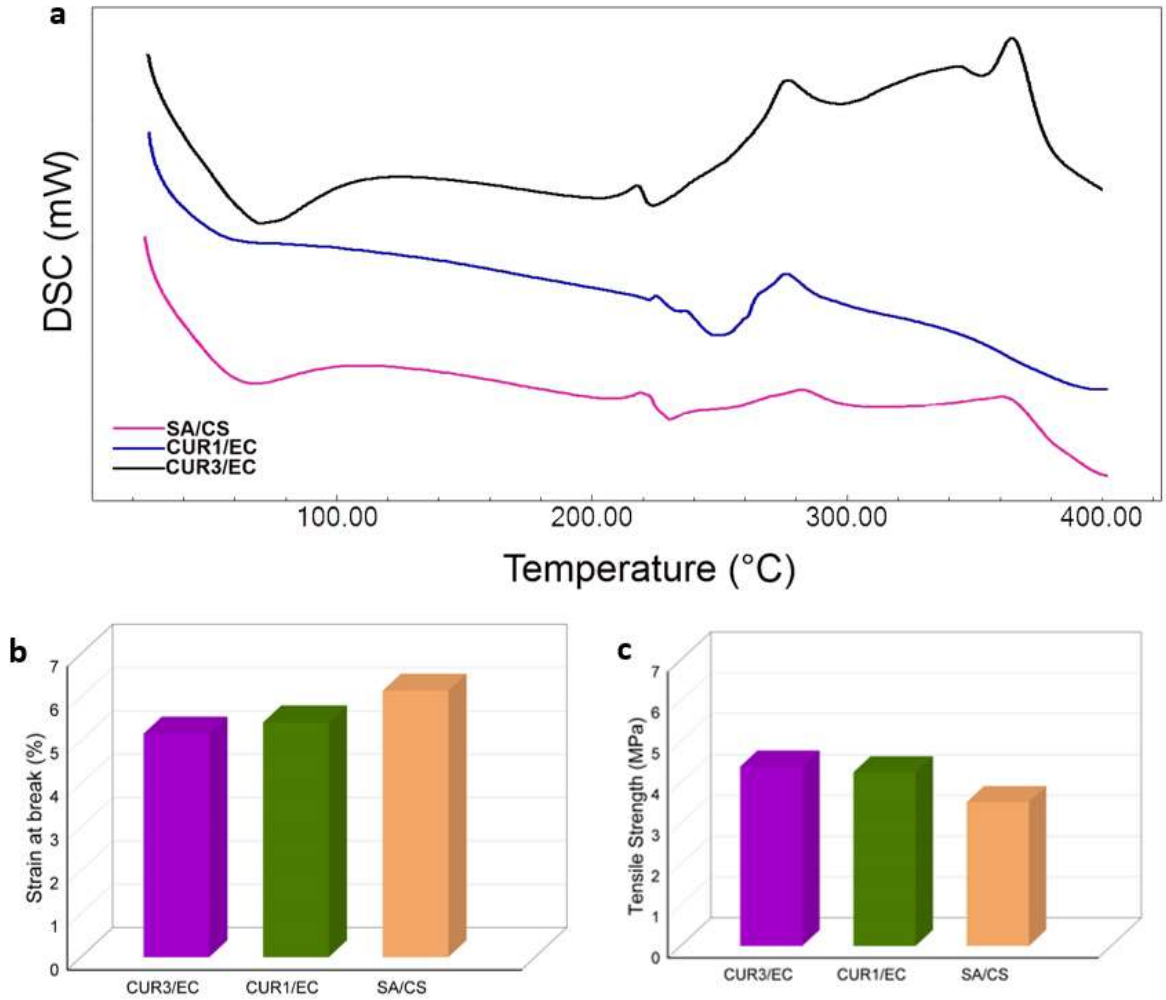


Fig. 4 - (a) DSC thermograms of SA/CS scaffold and CUR/EC-coated scaffolds reveal changes in thermal behavior following drug incorporation, indicating potential alterations in material properties. (b, c) Mechanical testing of the SA/CS scaffold and CUR/EC-coated scaffolds reveal distinct differences in the strain at break and tensile strength values.

3.3. Thermal behaviors of scaffolds

DSC is a valuable analytical technique utilized to assess physical transformations in materials concomitant with heat absorption. This study investigates the influence of CUR/EC nanoparticles on the melting point of scaffolds comprising SA and CS, thereby exploring the underlying intermolecular interactions. The DSC curves of unmodified scaffolds and CUR/EC-coated scaffolds, acquired within the temperature range of 25–400 °C, are depicted in Figure 4a. Given that the reported literature range for the melting point of CUR [35] falls within (172.85–187°C), an investigation was conducted using DSC to examine the thermogram of CUR in conjunction with SA/CS scaffolds. The scaffolds exhibited distinct peaks in their glass transition temperatures (T_g), with values of 62.3°C, 55.7°C, and 64.7°C for SA/CS, CUR1/EC, and CUR3/EC, respectively. These T_g values are consistent with the reported literature values for alginate-based materials [36]. The incorporation of CUR/EC nanoparticles onto the scaffolds resulted in a slight alteration of the Tg, indicating a subtle influence of CUR on the thermal behavior of the composite system. Furthermore, an exothermic peak is observed in the temperature range of 215-230°C for all the scaffolds, indicating the initiation of thermal degradation in the alginate-based scaffolds. Moreover, another exothermic peak is observed at temperatures between 275-280°C, suggesting the occurrence of two stages of thermal degradation. The weight loss observed in the first stage can be attributed to the volatilization of compounds, such as dehydration, while the weight loss observed in the second stage can be attributed to the decrosslinking of polymer networks [37]. Additional endothermic peaks within the temperature range of 220-250°C for all the scaffolds could potentially be linked to the desorption of water molecules bound to the hydrophilic groups present in alginate [34].

Particularly, the DSC analysis revealed the absence or disappearance of the distinctive

characteristic peaks associated with CUR. This observation suggests a potential alteration in the thermal behavior or interactions between CUR and the SA/CS scaffolds, leading to thermogram changes. The obtained results present strong evidence indicating the conversion of the crystalline structure of CUR into an amorphous state within the SA/CS scaffold. This conversion from the crystalline to the amorphous form is significant, as it enhances the solubility and stability of CUR. Furthermore, the absence of the characteristic CUR peak in the SA/CS scaffolds confirms the successful incorporation of the drug onto the scaffold. These findings underscore the potential of SA/CS scaffold as an effective matrix for the amorphous form of CUR, offering improved therapeutic performance.

3.4. Mechanical properties of scaffolds

The inherent characteristics of porous scaffolds, including their pore sizes and porosity, play a crucial role in dictating their mechanical attributes, as well as their capacity for nutrient transportation. Moreover, these structural properties have the potential to influence the subsequent performance of such scaffolds upon their integration within the site of a defect [38]. The mechanical characteristics of all scaffolds were evaluated utilizing a tensile testing apparatus. Figure 4(b,c) illustrates the strain at fracture and tensile strength of the respective scaffolds. The experimental outcomes reveal that CUR3/EC-coated scaffolds exhibit superior tensile strength when compared to SA/CS scaffolds, rendering them the most durable among the tested scaffolds. The coating of CUR/EC particles onto SA/CS scaffolds resulted in an enhancement of their tensile strength; however, it also led to a reduction in strain at break in comparison to scaffolds without CUR/EC particles.

The tensile strength results of the three scaffolds, namely SA/CS, CUR1/EC, and CUR3/EC, exhibited the following values, respectively: 3.18 ± 0.3 MPa, 3.96 ± 0.5 MPa, and 4.10 ± 0.8 MPa. In terms of strain at break percentages, the SA/CS scaffold demonstrated a value of 5.77 ± 1.2%, while CUR1/EC and CUR3/EC exhibited values of 5.22 ± 1.8% and 4.82 ± 2.2%, respectively. It can be posited that the inclusion of alginate-based scaffolds yields a favorable impact on the mechanical strength properties, primarily attributed to the crosslinking process subsequent to 3D printing. This crosslinking mechanism is pivotal in augmenting the strength values, consequently contributing to the measured MPa values. The obtained results play a pivotal role in assessing the flexibility and mechanical behavior of the product, which holds significant implications for its efficacy in facilitating successful wound treatment [39]. By comprehensively analyzing and interpreting these results, valuable insights can be gained regarding the product's ability to withstand mechanical stresses, adapt to dynamic wound environments, and maintain structural integrity, ultimately influencing its overall performance and therapeutic outcomes in wound healing.

3.5. Evaluation of Drug Release Kinetics from Scaffolds

The release of CUR from CUR1/EC-coated and CUR3/EC-coated scaffolds was investigated in a pH 7.4 PBS solution maintained at 37 °C. To determine the concentration of CUR, UV spectra were obtained by measuring the absorbance of six different CUR concentrations ranging from 0.2 to 1 mg/ml using a UV-Vis spectrophotometer, as shown in Figure 5(i). A standard calibration curve for CUR was established by measuring the absorbance values at 428 nm for various concentrations. These absorbance values were used to construct the calibration curve, as depicted in Figure 5(c). The drug release profiles of the investigated scaffolds are presented in Figure 5(f). The obtained results reveal distinct release patterns during the initial phase of the study. The differential release behavior and kinetics between the two scaffold formulations during the early stages of the release study were investigated. Specifically, the CUR3/EC-coated scaffolds exhibited a burst release of 65.3%, while the CUR1/EC-coated scaffolds demonstrated a comparatively lower burst release of 58.4%. Subsequently, over the course of the first 3 hours, the CUR1/EC-coated scaffolds released a total of 79.6% of the CUR, while the CUR3/EC-coated scaffolds released 85.7%. The CUR1/EC-coated and CUR3/EC-coated scaffolds exhibited sustained drug release profiles, with the cumulative drug release reaching 100% at 10 hours. This controlled release behavior demonstrates the ability of these scaffolds to release the drug over a period of time. The achieved drug release profiles indicate the potential of these scaffold formulations to serve as effective drug delivery systems, providing controlled and sustained release of CUR over clinically relevant timeframes, but since all scaffolds coated with CUR are fully released within 10 hours, the usage of CUR/EC-coated scaffolds through electrospraying might not exhibit the capability to regulate the desired spatiotemporal drug delivery pattern finely. Consequently, it leads to substantial initial drug releases and high-dose administrations of CUR, which may potentially give rise to severe adverse effects [5].

The mathematical modeling of drug release kinetics assumes a paramount role in the comprehensive analysis of drug release dynamics. By elucidating the underlying mechanisms, optimizing formulation parameters, and predicting the in vivo performance of drug delivery systems, mathematical modeling aids in advancing our

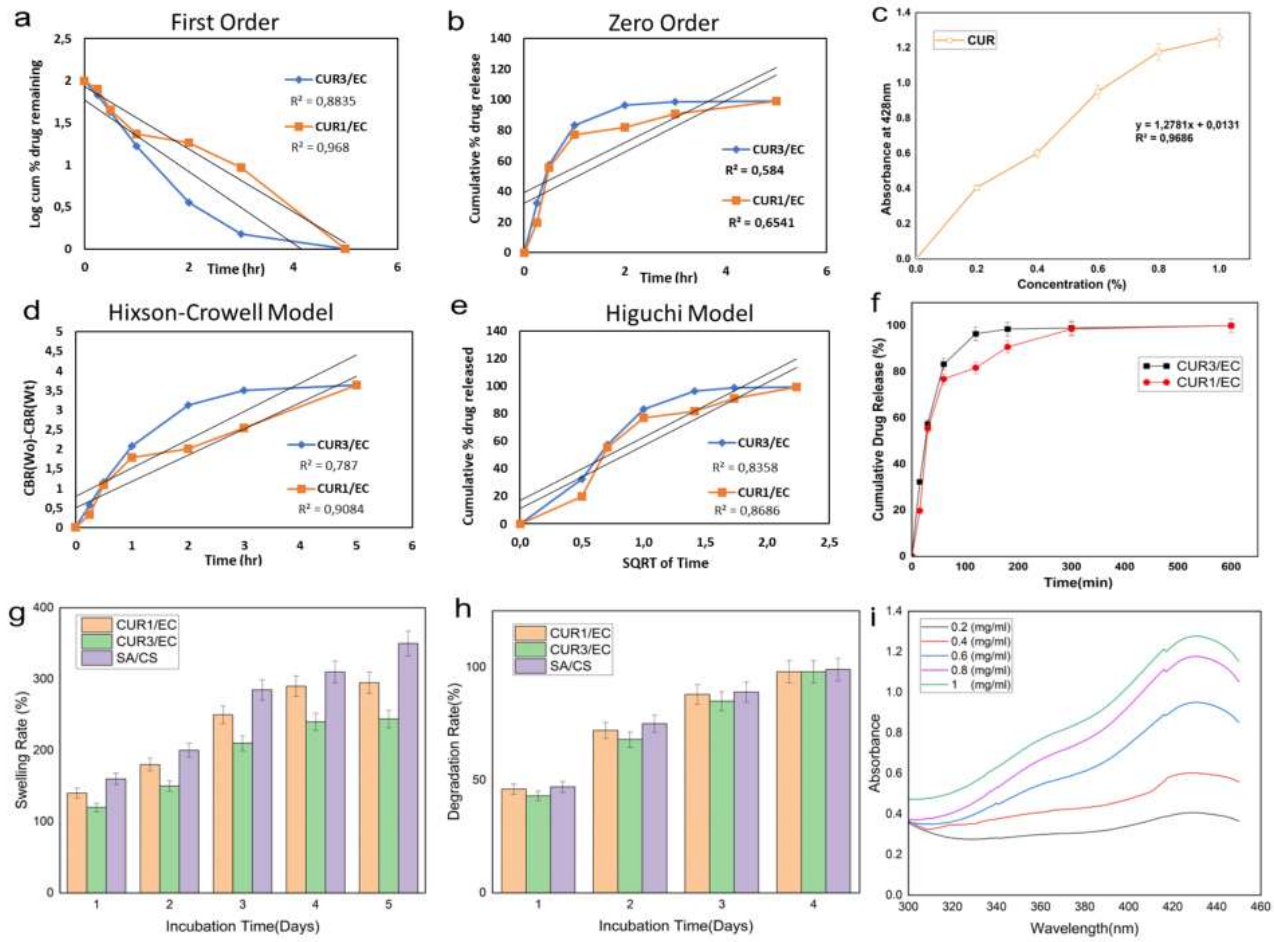


Fig. 5 - Comprehensive characterization of drug release mechanisms, kinetics, swelling behavior, and degradation rate of scaffolds and CUR/EC-coated scaffolds. The study presents results for first-order (a), zero-order (b), absorbance at 428nm for CUR in a standard calibration graph (c), Hixson-Crowell (d), Higuchi model (e), a cumulative drug-release graph of CUR from the scaffolds (f), swelling behavior (g), and degradation rate (h) of the scaffolds. Additionally, the absorbance graph of CUR at different concentrations (i) is presented to provide further insights into the drug release behavior.

understanding and enhancing the efficacy of drug release processes [40]. In order to investigate the release kinetics of CUR from the scaffolds, four distinct mathematical models were employed. Figure 4 (a, b, d, e) presents the regression coefficients (R^2) corresponding to these models, along with specific details regarding each model. The analysis revealed that CUR1/EC exhibited the highest degree of conformity with the first-order model (R^2: 96.9 %), indicating a favorable fit. Moreover, the Hixson-Crowell (R^2: 90.8 %) and Higuchi models (R^2: 86.8 %) displayed comparatively better agreement with the experimental data. With an increase in CUR concentration, a notable decrease in the values representing the kinetic patterns of CUR release from the CUR3/EC-coated scaffolds can be observed. Specifically, the first-order (R^2: 88.4 %), Higuchi (R^2: 83.6 %), and Hixson-Crowell (R^2: 78.7%) models remain the most suitable representations for the release kinetics of CUR, albeit with decreasing release values as the concentration of CUR increases. In contrast, the zero-order model exhibited the least agreement for both CUR1/EC and CUR3/EC with the observed release kinetics of CUR from the scaffolds. In the context of CUR/EC-coated scaffolds with varying concentrations, it was observed that the Hixson-Crowell model exhibited superior suitability compared to the Higuchi model as the CUR concentration increased. This finding suggests that the release mechanism from these scaffolds is influenced by factors beyond pure diffusion, as implied by the evolving drug release behavior observed in the experimental data.

3.6. Swelling and degradation behaviors of scaffolds

The immersion method was employed to ascertain the absorption capacity of all scaffolds. The capacity for water absorption facilitates the transportation of vital nutrients and oxygen to the internal regions of the fabricated scaffolds [41]. As widely recognized, the primary material utilized in the 3D printed scaffolds in this research was SA. Upon surveying the literature, it is evident that SA-based scaffolds typically exhibit remarkably high water absorption capacity, rendering them highly desirable for applications in wound healing, owing to this notable attribute [42]. In Figure 5(g), the

swelling behavior of both the scaffolds and CUR-coated scaffolds was monitored over a 5-day period. Remarkably, even at the conclusion of the first day, a significant swelling capacity of approximately 120-150% was observed. After 5 days, the SA/CS scaffold exhibited an impressive swelling capacity of 342%, while the CUR1/EC-coated and CUR3/EC-coated scaffolds reached swelling capacities of 287% and 230%, respectively. Notably, when considering their swelling capacity, the scaffolds coated with CUR/EC demonstrated comparatively lower swelling properties, particularly in the case of high CUR concentrations, where a reduced swelling capacity was observed compared to drug-free scaffolds. This outcome can be attributed to the hydrophobic nature of CUR[43], which suggests that it absorbs less water compared to SA/CS scaffold.

Additionally, upon analyzing the swelling capacities among the CUR/EC-coated scaffolds, a progressive increase was observed over time. This phenomenon can be attributed to the gradual dispersion of CUR/EC nanoparticles in the surrounding PBS solution, resulting in a diminishing presence of the hydrophobic drug on the scaffold and subsequently augmenting the swelling capacity. The findings indicate that all scaffold demonstrates stability and possesses a substantial water absorption capacity suitable for tissue engineering applications, particularly in the production of biomaterials for wound healing purposes.

The process of scaffold degradation assumes a crucial role in the field of tissue engineering, contributing significantly to the development and refinement of novel tissue engineering strategies [44]. An essential attribute inherent to scaffolds is their ability to undergo degradation, resulting in a concomitant reshaping process that harmonizes with the dynamic formation of new tissue [45]. To enhance the aqueous solubility and stability of CUR, a compound known for its high hydrophobicity and chemical instability, it was encapsulated within EC nanoparticles. This encapsulation strategy aimed to overcome the inherent challenges associated with CUR's poor solubility in aqueous environments and susceptibility to degradation. The incorporation of CUR/EC nanoparticles onto the scaffolds exhibited minimal influence on the degradation process, as evidenced by the complete disintegration of the scaffolds within a period of 4 days in Figure 5(h). By the end of the initial day, the degradation level of all scaffolds approached approximately 50%, indicating that over half of the scaffolds had undergone degradation within this time frame. Notably, CUR3/EC-coated scaffolds displayed a slightly lesser degree of degradation compared to the other groups within the same time frame. It may reduce scaffold disintegration due to heightened local activity of CUR nanoparticles. Additionally, the encapsulation of CUR within EC nanoparticles might offer protective benefits, shielding the drug from degradation and enhancing its overall stability during storage and transportation. This approach demonstrates the potential of nanoparticle-based delivery systems for addressing the stability and solubility limitations of hydrophobic and chemically sensitive compounds like CUR. Moreover, considering the degradation in relation to the overall scaffold weight, it is apparent that the layers of nanoparticles undergo a concomitant degradation process in tandem with the scaffold, indicating an integrated degradation pattern.

3.7. Cell culture assay

Figure 6 presents the cytotoxicity evaluation of the fibers on L929 mouse fibroblast cells at 1, 3, and 7 days, employing the XTT assay. Fibroblasts, the primary cellular constituents responsible for the modulation of extracellular matrix (ECM) protein synthesis [46], assume a pivotal role in orchestrating essential mechanisms crucial for proficient wound healing. These multifaceted cells actively participate in various processes vital for the progression of normal wound healing, encompassing the degradation of fibrin clots, synthesis of novel ECM components to provide structural support to other cell populations involved in effective wound repair, and the facilitation of wound contraction [47].

The results reveal that the viability of the cells exposed to the scaffolds exhibited no statistically significant difference compared to the control group. A comparative analysis of experimental data with the negative control group showed that all scaffolds exhibited significantly higher cell viability compared to the control group. Moreover, no discernible inhibition of cell proliferation was observed across days 1, 3, and 7. This implies that the presence of the scaffolds did not adversely affect the survival and growth of the fibroblast cells over the entire duration of the experiment. As the concentration increased in all scaffolds, a marginal decline in cell viability was observed. However, specifically in the SA/CS scaffold, at a concentration of 3 mg/ml, the viability decreased to 93%, which fell below the viability of the control group. The scaffolds incorporating CUR/EC displayed a noticeable disparity in viability at the 1-day mark, which subsequently diminished at 3 and 7 days. However, overall, the viability of CUR/EC-coated scaffolds was better.

At the initial 24-hour time point, the CUR1/EC 0.5 mg/ml concentration demonstrated the highest level of viability at an impressive 115.4%, surpassing other concentrations. It was closely followed by the CUR3/EC 0.1 mg/ml concentration, exhibiting a viability of 113.3%, and the SA/CS scaffold at the 0.5 mg/ml concentration, which

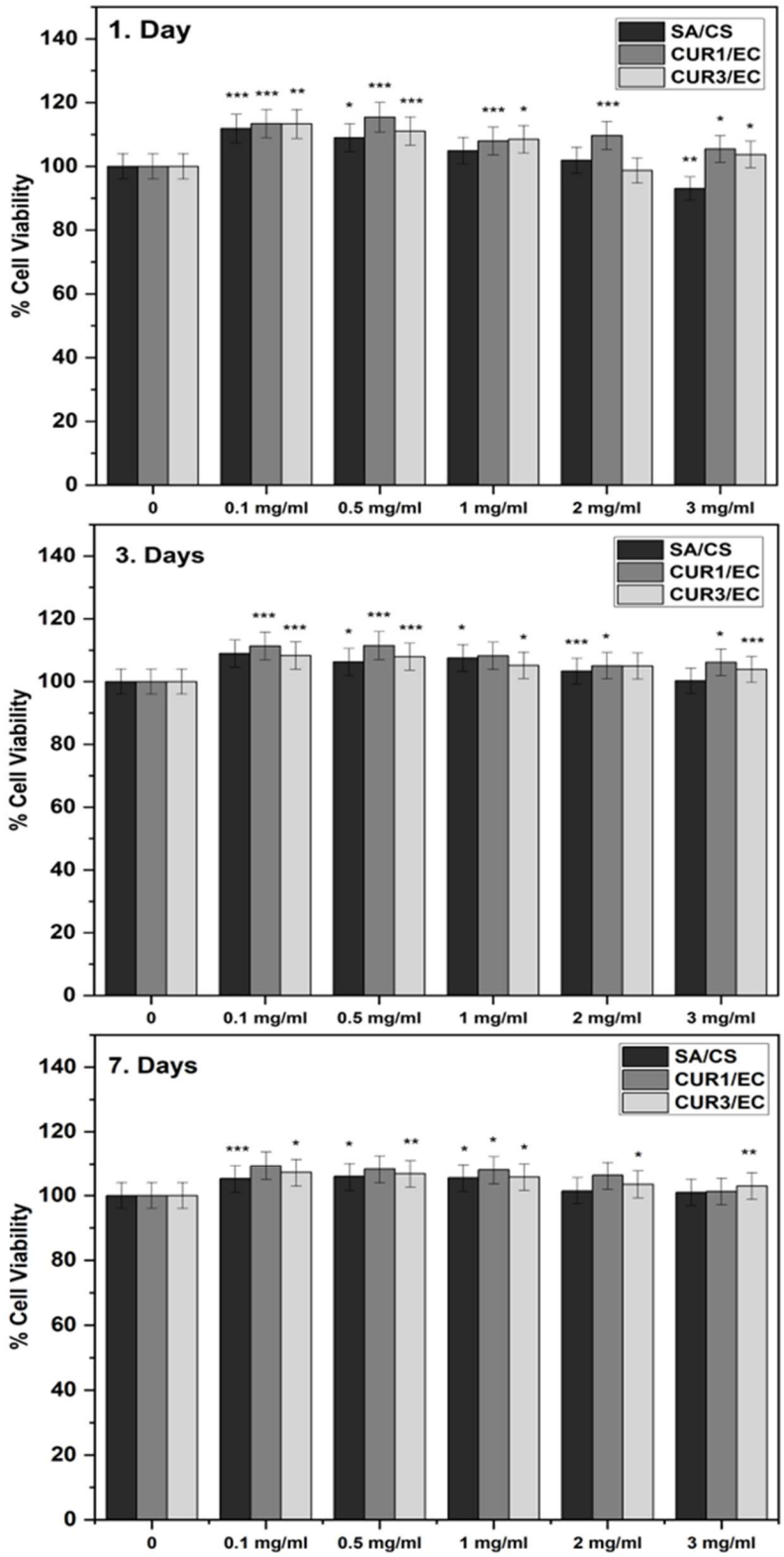


Fig. 6 - Assessment of scaffold biocompatibility through XTT viability assays at 1, 3, and 7 days post-seeding. Differences were considered statistically significant if $p < 0.05$*, $p < 0.005$**, and $p < 0.001$*** compared to the control.

achieved commendable viability of 109%. Subsequently, on the third day, the CUR1/EC 0.5 mg/ml concentration maintained its prominence with viability of 111.5%, signifying its sustained impact. The SA/CS scaffold at the 0.1 mg/ml concentration also showed noteworthy viability at 108.9%, while the CUR3/EC 0.1 mg/ml concentration maintained respectable viability of 108.3%. Shifting to the seventh day, the CUR1/EC 0.1 mg/ml concentration exhibited the highest viability among all conditions, displaying a robust viability of 109.4%. The CUR3/EC concentration followed closely behind, which retained a commendable viability of 107.2%. Particularly, the SA/CS scaffold at the 0.5 mg/ml

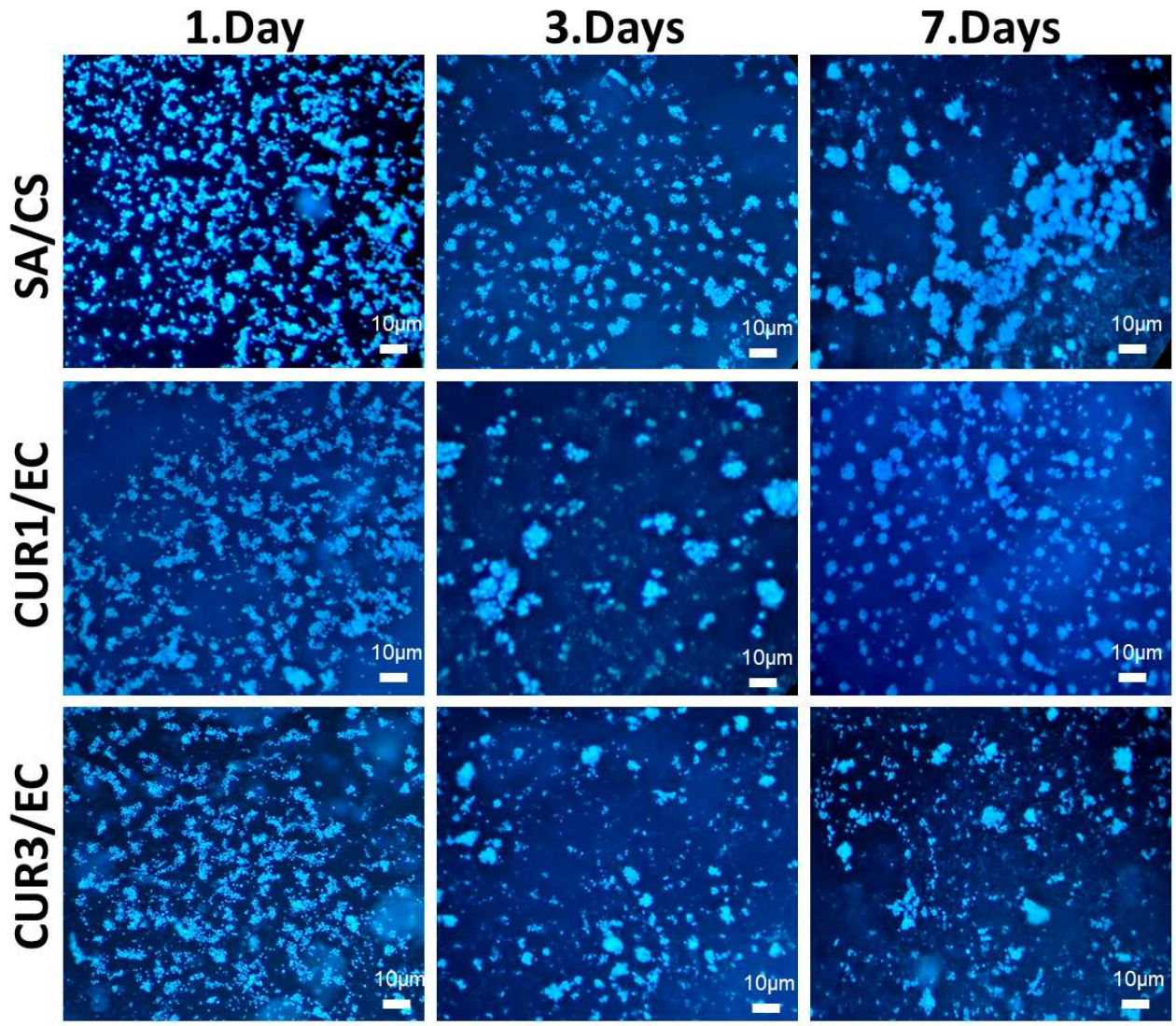


Fig.7- Visualization of cellular attachment and proliferation on scaffolds using DAPI staining and fluorescent microscopy at 1, 3, and 7 days. DAPI is a fluorescent stain that binds to DNA, allowing for the visualization of cell nuclei. These images provide valuable insights into the temporal dynamics of cell attachment and proliferation on the scaffolds.

concentration showcased its highest viability at 105.9%, demonstrating its potential as a viable platform for sustained cellular survival.

According to ISO standard 10993-5, if the relative cell viability of the highest concentration of the scaffolds is equal to or exceeds 70% compared to the control group, it is deemed that the scaffold exhibits non-cytotoxic properties. Thus, it becomes apparent that all scaffolds can be cautiously applied at the wound site without posing any risk of cytotoxicity. These findings indicate the absence of cytotoxic effects and suggest favorable biocompatibility of the tested scaffolds.

Cell viability on the scaffolds was assessed on days one, three, and seven using fluorescence microscopy to observe the survival of the cells. The nuclei of DAPI-stained fibroblasts are shown in Figure 7. Based on the fluorescent images, it was evident that the 3D-printed scaffolds exhibited a higher density and a more dispersed arrangement of cells on the first day compared to the subsequent days. Observations reveal a reduced occurrence of aggregation within the fluorescent images of the scaffolds incorporated with CUR/EC, particularly after a span of 7 days.

SEM analysis was employed to investigate the interplay between the scaffold materials and fibroblast cells, as well as to assess the morphological characteristics. The observations were made on the first, third, and seventh days of incubation. Figure 8 visually presents the findings, illustrating that the scaffolds demonstrated favorable fibroblast attachment and proliferation throughout the incubation period. Enhanced adhesion and proliferation of cells on the scaffold were prominently observed in scaffolds coated with CUR/EC. Within a 7-day timeframe, a noticeable augmentation in cell spreading and clustering was determined in CUR3/EC-coated scaffolds. Similar to these results, Ravanfar et al. observed a,

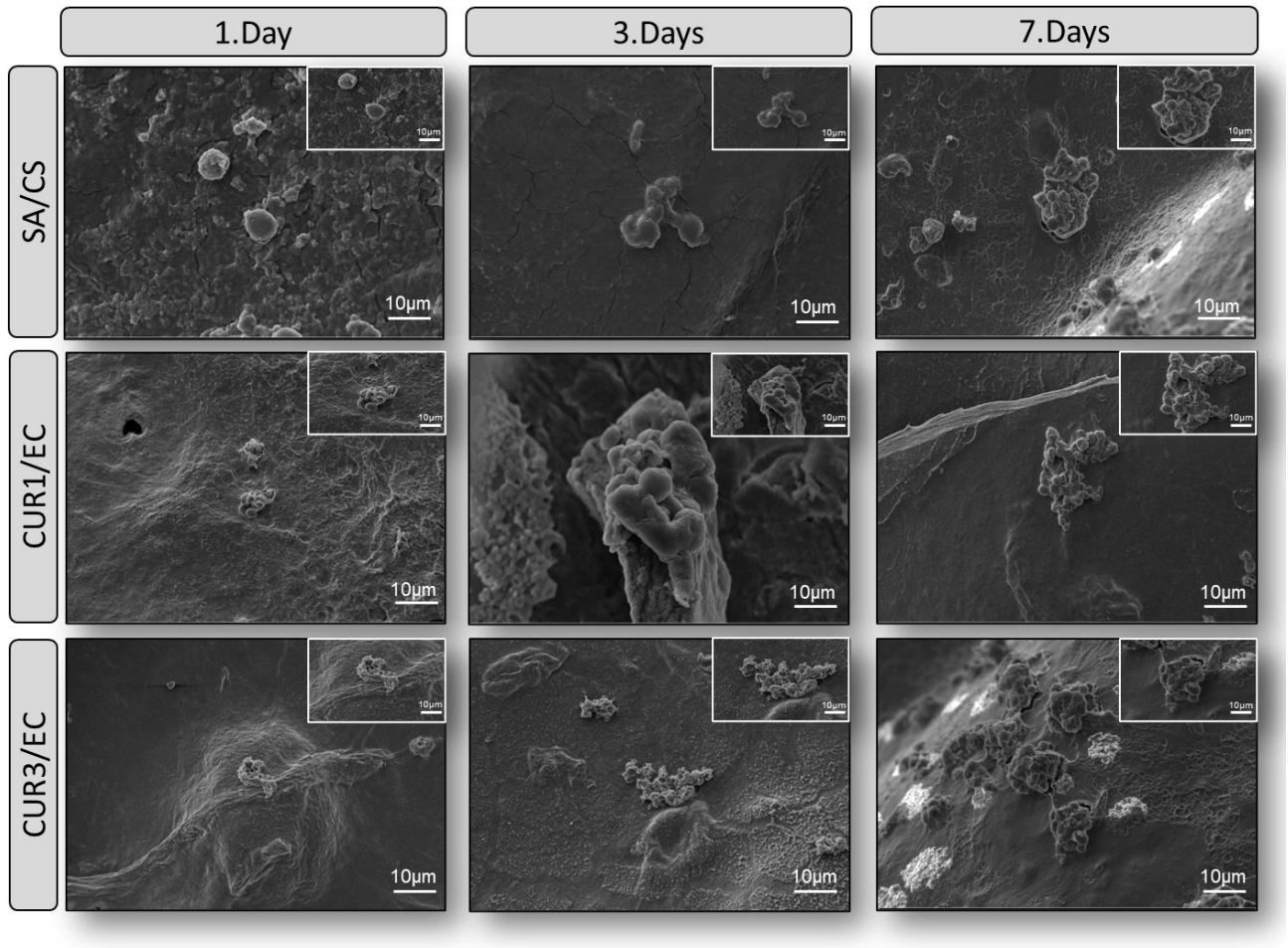


Fig. 8- SEM images of scaffolds after 1, 3, and 7 days of treatment. The scale of the images is 10 µm, providing high-resolution views of the scaffold surface morphology and structure over time. These images offer valuable insights into how the scaffolds respond to cellular interactions.

significant acceleration of cellular proliferation and a shortened inflammatory phase following CUR/EC addition [48]. In the CUR3/EC-coated scaffold conspicuous and luminous structures are observed in close proximity to the cells residing on the scaffold. These distinct bright structures are attributed to CUR, as CUR possesses multiple phenolic groups on its surface, imparting a positive charge. Specifically, turmeric, from which CUR is derived, exhibits antioxidant properties and is rich in phenolic groups that bear positively charged hydrogen atoms [49].

4. Conclusion

An optimal scaffold should establish a homeostatic milieu conducive to expediting diabetic wound healing while concurrently regulating oxidative stress, enzymatic activities, and hypoxic conditions. Furthermore, it should impart mechanical support and mitigate the risk of infection, thereby effectively addressing the multifaceted challenges inherent to the wound microenvironment. This investigation elucidates the potential of incorporating CUR/EC nanoparticles onto scaffolds to facilitate sustained release in the context of diabetic wounds. CUR3/EC exhibited the most rapid release, surpassing CUR1/EC, with an impressive 85.7% release observed within the initial 3-hour period. All CUR/EC-coated scaffolds revealed an outstanding outcome in terms of cell viability, with rates exceeding 100%. Furthermore, SEM and DAPI images provided supportive evidence for the adhesion and proliferation of fibroblast cells on the scaffold. Regarding the mechanical assessment, it is evident that the inclusion of CUR/EC nanoparticles has notably enhanced the mechanical robustness of the scaffolds. Specifically, the tensile strength of the CUR3/EC-coated scaffold demonstrated a substantial increase, reaching approximately 4.10 MPa. These findings underscore the feasibility and versatility of employing CUR/EC-coated scaffolds as a therapeutic approach for diabetic wound management, thereby paving the way for future advancements in this field.

Data availability

The raw data will be made available upon request.

REFERENCES

1. Zhao H, Huang J, Li Y, Lv X, Zhou H, Wang H, et al. ROS-scavenging hydrogel to promote healing of bacteria infected diabetic wounds. Biomaterials. 2020 Nov 1;258:120286.
2. Ding X, Yu Y, Li W, Zhao Y. In situ 3D-bioprinting MoS2 accelerated gelling hydrogel scaffold for promoting chronic diabetic wound healing. Matter. 2023 Mar 1;6(3):1000–14.
3. Kant V, Gopal A, Pathak NN, Kumar P, Tandan SK, Kumar D. Antioxidant and anti-inflammatory potential of curcumin accelerated the cutaneous wound healing in streptozotocin-induced diabetic rats. Int Immunopharmacol [Internet]. 2014 [cited 2023 May 16];20(2):322–30. Available from: https://pubmed.ncbi.nlm.nih.gov/24675438/
4. Harmanci S, Dutta A, Cesur S, Sahin A, Gunduz O, Kalaskar DM, et al. Production of 3D Printed Bi-Layer and Tri-Layer Sandwich Scaffolds with Polycaprolactone and Poly (vinyl alcohol)-Metformin towards Diabetic Wound Healing. Polymers (Basel) [Internet]. 2022 Dec 1 [cited 2023 May 16];14(23):5306. Available from: https://www.mdpi.com/2073-4360/14/23/5306/htm
5. Pop MA, Almquist BD. Biomaterials: A potential pathway to healing chronic wounds? Exp Dermatol [Internet]. 2017 Sep 1 [cited 2023 May 16];26(9):760–3. Available from: https://onlinelibrary.wiley.com/doi/full/10.1111/exd.13290
6. Place ES, Evans ND, Stevens MM. Complexity in biomaterials for tissue engineering. Nat Mater 2009 86 [Internet]. 2009 [cited 2023 May 16];8(6):457–70. Available from: https://www.nature.com/articles/nmat2441
7. Zheng G, Liu X, Wang X, Chen L, Xie H, Wang F, et al. Improving stability and biocompatibility of alginate/chitosan microcapsule by fabricating bi-functional membrane. Macromol Biosci. 2014;14(5):655–66.
8. Machluf M. Alginate – Chitosan Complex Coacervation for Cell Encapsulation : Effect on Mechanical Properties and on Long-Term Viability. 2006;82:570–9.
9. Topal F, Ertas B, Guler E, Gurbuz F, Ozcan GS, Aydemir O, et al. A novel multi-target strategy for Alzheimer's disease treatment via sublingual route: Donepezil/memantine/curcumin-loaded nanofibers. Biomater Adv. 2022 Jul 1;138:212870.
10. Kumari A, Raina N, Wahi A, Goh KW, Sharma P, Nagpal R, et al. Wound-Healing Effects of Curcumin and Its Nanoformulations: A Comprehensive Review. Pharmaceutics [Internet]. 2022 Nov 1 [cited 2023 May 16];14(11):2288. Available from: /pmc/articles/PMC9698633/
11. Ruiz A, Baños G, El-Hafidi M, Pérez-Torres I, Ruiz-Ramírez A. Hibiscus sabdariffa Linnaeus (Malvaceae), curcumin and resveratrol as alternative medicinal agents against metabolic syndrome. ingentaconnect.com [Internet]. 2012 [cited 2023 May 16];(11):25. Available from: https://www.ingentaconnect.com/content/ben/chamc/2013/00000011/00000001/art00006
12. Alizadeh M, Kheirouri S. Curcumin reduces malondialdehyde and improves antioxidants in humans with diseased conditions: A comprehensive meta-analysis of randomized controlled trials. Biomed. 2019 Dec 1;9(4):10–22.
13. Urbán-Morlán Z, Mendoza-Elvira SE, Hernández-Cerón RS, Alcalá-Alcalá S, Ramírez-Mendoza H, Ciprián-Carrasco A, et al. Preparation of ethyl cellulose nanoparticles by Solvent-Displacement using the conventional method and a recirculation system. J Mex Chem Soc. 2015;59(3):173–80.
14. Kibbelaar HVM, Dekker RI, Morcy A, Kegel WK, Velikov KP, Bonn D. Ethyl cellulose nanoparticles as stabilizers for Pickering emulsions. Colloids Surfaces A Physicochem Eng Asp. 2022 May 20;641:128512.
15. Prasertmanakit S, Praphairaksit N, Chiangthong W, Muangsin N. Ethyl cellulose microcapsules for protecting and controlled release of folic acid. AAPS PharmSciTech. 2009 Dec;10(4):1104–12.
16. Abdel-Mottaleb M, Moulari B, … AB-E journal of, 2012 undefined. Nanoparticles enhance therapeutic outcome in inflamed skin therapy. Elsevier [Internet]. [cited 2023 May 15]; Available from: https://www.sciencedirect.com/science/article/pii/S0939641112001932?casa_token=EcmOfIXH1y8AAAAA:3TJEj-RN_FNKz471LmyHFPvl0VLW3VKMvJ-pT03MS2dTK6_lIUh6Ac2l7IydjrpKKok5xGti3R4
17. Li KJ, Guan GL, Zhu JX, Wu H, Sun QJ. Antibacterial activity and mechanism of a laccase-catalyzed chitosan-gallic acid derivative against Escherichia coli and Staphylococcus aureus. Food Control. 2019;96:234–43.
18. Zhou W, Stoyanov S, Jin H, Zhou W, Cao J, Stoyanov SD, et al. Super stable foams stabilized by colloidal ethyl cellulose particles. pubs.rsc.org [Internet]. [cited 2023 May 15]; Available from: https://pubs.rsc.org/en/content/articlehtml/2012/sm/c1sm06518a
19. Zou L, Xie A, Zhu Y, McClements DJ. Cereal proteins in nanotechnology: formulation of encapsulation and delivery systems. Curr Opin Food Sci [Internet]. 2019;25:28–34. Available from: https://doi.org/10.1016/j.cofs.2019.02.004
20. Diagnosis D, Shakeri S, Ashrafizadeh M, Zarrabi A, Roghanian R. Multifunctional Polymeric Nanoplatforms for Brain. Biomedicines. 2020.
21. Nasery MM, Abadi B, Poormoghadam D. Curcumin Delivery Mediated by Bio-Based. 2020;1–28.
22. Aydin S, Kabaoglu I, Guler E, Topal F, Hazar-Yavuz AN, Ekentok C, et al. A Comparison Study of Fiber Diameter's Effect on Characteristic Features of Donepezil/Curcumin-Loaded Polycaprolactone/Polylactic Acid Nanofibers. Macromol Mater Eng. 2022;307(5):1–15.
23. Castel-Molieres M, Conzatti G, Torrisani J, Rouilly A, Cavalie S, Carrere N, et al. Influence of Homogenization Technique and Blend Ratio on Chitosan/Alginate Polyelectrolyte Complex Properties. J Med Biol Eng. 2018;38(1):10–21.
24. Ayran M, Dirican AY, Saatcioglu E, Ulag S, Sahin A, Aksu B, Croitoru AM, Ficai D, Gunduz O, Ficai A. 3D-Printed PCL Scaffolds Combined with Juglone for Skin Tissue Engineering. Bioengineering. 2022 Aug 30;9(9):427.
25. Aranci K, Uzun M, Su S, Cesur S, Ulag S, Amin A, et al. 3D Propolis-Sodium Alginate Scaffolds: Influence on Structural Parameters, Release Mechanisms, Cell Cytotoxicity and Antibacterial Activity. Mol 2020, Vol 25, Page 5082 [Internet]. 2020 Nov 2 [cited 2023 May 13];25(21):5082. Available from: https://www.mdpi.com/1420-3049/25/21/5082/htm
26. Ayran M, Karabulut H, Deniz KI, Akcanli GC, Ulag S, Croitoru A-M, et al. Electrically Triggered Quercetin Release from Polycaprolactone/Bismuth Ferrite Microfibrous Scaffold for Skeletal Muscle Tissue. Pharmaceutics [Internet]. 2023 Mar 11 [cited 2023 May 12];15(3):920. Available from: https://pubmed.ncbi.nlm.nih.gov/36986781/
27. Pilavci E, Ayran M, Ulubay D, Kaya E, Tinaz G, Bingol Ozakpinar O, et al. Fabrication and characterization of electrospun GelMA/PCL/CS nanofiber composites for wound dressing applications. https://doi.org/101177/08839115221138777 [Internet]. 2022 Dec 7 [cited 2023 May 11];38(1):3–24. Available from: https://journals.sagepub.com/doi/abs/10.1177/08839115221138777

28. ISO 10993-5:2009(en), Biological evaluation of medical devices — Part 5: Tests for in vitro cytotoxicity [Internet]. [cited 2023 May 9]. Available from: https://www.iso.org/obp/ui/#iso:std:iso:10993:-5:ed-3:v1:en
29. Ilhan E, Ulag S, Sahin A, Yilmaz BK, Ekren N, Kilic O, et al. Fabrication of tissue-engineered tympanic membrane patches using 3D-Printing technology. J Mech Behav Biomed Mater [Internet]. 2021;114(March 2020):104219. Available from: https://doi.org/10.1016/j.jmbbm.2020.104219
30. Lu H, Oh HH, Kawazoe N, Yamagishi K, Chen G. PLLA–collagen and PLLA–gelatin hybrid scaffolds with funnel-like porous structure for skin tissue engineering. http://www.tandfonline.com/action/journalInformation?show=aimsScope&journalCode=tsta20#VmBmuzZFCUk [Internet]. 2012 Dec [cited 2023 May 28];13(6). Available from: https://www.tandfonline.com/doi/abs/10.1088/1468-6996/13/6/064210
31. Oh SH, Park IK, Kim JM, Lee JH. In vitro and in vivo characteristics of PCL scaffolds with pore size gradient fabricated by a centrifugation method. Biomaterials. 2007 Mar 1;28(9):1664–71.
32. Ma L, Gao C, Mao Z, Zhou J, Shen J, Hu X, et al. Collagen/chitosan porous scaffolds with improved biostability for skin tissue engineering. Biomaterials [Internet]. 2003 [cited 2023 May 28];24(26):4833–41. Available from: https://www.researchgate.net/publication/9062621_Collagenchitosan_porous_scaffolds_with_improved_biostability_for_skin_tissue
33. Chen J, Qin X, Zhong S, Chen S, Su W, Liu Y. Characterization of Curcumin/Cyclodextrin Polymer Inclusion Complex and Investigation on Its Antioxidant and Antiproliferative Activities. Molecules [Internet]. 2018 [cited 2023 May 26];23(5). Available from: https://pubmed.ncbi.nlm.nih.gov/29762477/
34. Bagre AP, Jain K, Jain NK. Alginate coated chitosan core shell nanoparticles for oral delivery of enoxaparin: in vitro and in vivo assessment. Int J Pharm [Internet]. 2013;456(1):31–40. Available from: http://dx.doi.org/10.1016/j.ijpharm.2013.08.037
35. Mashaqbeh H, Obaidat R, Al-Shar'i N. Evaluation and characterization of curcumin-β-cyclodextrin and cyclodextrin-based nanosponge inclusion complexation. Polymers (Basel) [Internet]. 2021 Dec 1 [cited 2023 May 26];13(23). Available from: /pmc/articles/PMC8658939/
36. Diana MI, Selvasekarapandian S, Selvin PC, Krishna MV. A physicochemical elucidation of sodium perchlorate incorporated alginate biopolymer: toward all-solid-state sodium-ion battery. J Mater Sci [Internet]. 2022 May 1 [cited 2023 May 29];57(17):8211–24. Available from: https://link.springer.com/article/10.1007/s10853-022-07185-w
37. Siddaramaiah, Swamy TMM, Ramaraj B, Lee JH. Sodium alginate and its blends with starch: Thermal and morphological properties. J Appl Polym Sci [Internet]. 2008 Sep 15 [cited 2023 May 29];109(6):4075–81. Available from: https://onlinelibrary.wiley.com/doi/full/10.1002/app.28625
38. Stangl R, Rinne B, Kastl S, Hendrich C, Stangl R. THE INFLUENCE OF PORE GEOMETRY IN CP TI-IMPLANTS-A CELL CULTURE INVESTIGATION. 2001;2:1–9.
39. Straccia MC, Romano I, Oliva A, Santagata G, Laurienzo P. Crosslinker effects on functional properties of alginate/N-succinylchitosan based hydrogels. Carbohydr Polym. 2014 Aug 8;108(1):321–30.
40. Elmas A, Akyüz G, Bergal A, Andaç M, Andaç Ö. Mathematical Modelling of Drug Release. Res Eng Struct Mat. 2020;6(4):327–50.
41. Peter M, Binulal NS, Soumya S, Nair S V., Furuike T, Tamura H, et al. Nanocomposite scaffolds of bioactive glass ceramic nanoparticles disseminated chitosan matrix for tissue engineering applications. Carbohydr Polym. 2010 Jan 20;79(2):284–9.
42. Ilhan E, Cesur S, Guler E, Topal F, Albayrak D, Guncu MM, et al. Development of Satureja cuneifolia-loaded sodium alginate/polyethylene glycol scaffolds produced by 3D-printing technology as a diabetic wound dressing material. Int J Biol Macromol. 2020 Oct 15;161:1040–54.
43. Shen L, Liu CC, An CY, Ji HF. How does curcumin work with poor bioavailability? Clues from experimental and theoretical studies. Sci Reports 2016 61 [Internet]. 2016 Feb 18 [cited 2023 May 21];6(1):1–10. Available from: https://www.nature.com/articles/srep20872
44. Zhang H, Zhou L, Zhang W. Control of scaffold degradation in tissue engineering: a review. Tissue Eng Part B Rev [Internet]. 2014 Oct 1 [cited 2023 May 21];20(5):492–502. Available from: https://pubmed.ncbi.nlm.nih.gov/24547761/
45. Lyu SP, Schley J, Loy B, Lind D, Hobot C, Sparer R, et al. Kinetics and time-temperature equivalence of polymer degradation. Biomacromolecules [Internet]. 2007 Jul [cited 2023 May 21];8(7):2301–10. Available from: https://pubmed.ncbi.nlm.nih.gov/17579477/
46. Tettamanti G, Grimaldi A, Rinaldi L, Arnaboldi F, Congiu T, Valvassori R, et al. The multifunctional role of fibroblasts during wound healing in Hirudo medicinalis (Annelida, Hirudinea). Biol Cell [Internet]. 2004 Aug 1 [cited 2023 May 28];96(6):443–55. Available from: https://onlinelibrary.wiley.com/doi/full/10.1016/j.biolcel.2004.04.008
47. Karri VVSR, Kuppusamy G, Talluri SV, Mannemala SS, Kollipara R, Wadhwani AD, et al. Curcumin loaded chitosan nanoparticles impregnated into collagen-alginate scaffolds for diabetic wound healing. Int J Biol Macromol [Internet]. 2016;93:1519–29. Available from: http://dx.doi.org/10.1016/j.ijbiomac.2016.05.038
48. Ravanfar K, Amniattalab A, Mohammadi R. Curcumin-Polyethylene Glycol Loaded on Chitosan-Gelatin Nanoparticles Enhances Burn Wound Healing in Rat. J Burn Care Res [Internet]. 2022 Nov 2 [cited 2023 May 28];43(6):1399–409. Available from: https://academic.oup.com/jbcr/article/43/6/1399/6568529
49. Suprianto T, Winarto, Wijayanti W, Wardana ING. Synergistic effect of curcumin and activated carbon catalyst enhancing hydrogen production from biomass pyrolysis. Int J Hydrogen Energy. 2021 Feb 8;46(10):7147–64.

****